An experimental investigation of a high Reynolds number turbulent wake generated by a vehicle-like bluff body

Samaresh Midya* and Sean Symon
Aerodynamics and Flight Mechanics,
Faculty of Engineering and Physical Sciences,
University of Southampton, Southampton SO17 1BJ, United Kingdom

(Dated: June 26, 2025)

Abstract

This study uses stereo-particle image velocimetry to describe the wake behind a multi-wake model at a Reynolds number of 5.64×10^5 based on the model length L_x. All three velocity components are measured in cross-stream planes at various streamwise locations starting from the trailing edge of the model. The time-averaged, three-dimensional flow is reconstructed from the planar measurements, and three important regions in the wake are identified. The near-wake is dominated by a separation bubble that forms immediately downstream of the model. Shear layers, which detach from the sides of the model, morph into a single connected 'bound vortex' that stays inside the separation bubble and dominates the flow up to $x/L_x \approx 0.4$. The far-wake is mainly influenced by four corner vortices that originate from the upper and lower rear slant edges. In the near-wake region, the corner vortices enhance the inward mass and momentum transfer in the vertical direction and oppose them in the spanwise direction. As such, they warp the shape of the separation bubble although their overall effect on the internal flow within the separation bubble is minor. In the far wake, they redistribute the momentum in the vertical-spanwise plane. Their induced flow reduces the momentum deficit in the central streamwise-vertical plane relative to off-center planes. It can be concluded that it is the corner vortices which dominate the far-wake and that they remain coherent several body lengths behind the vehicle. Similar to the Ahmed body, the slant angles play a major role on the evolution of the wake which has implications for reducing drag.

I. INTRODUCTION

Flows past bluff bodies result in highly three-dimensional wakes with features such as a turbulent boundary layer, separation and reattachment on the vehicle surface, and massive flow separation at the rear surface resulting in a large wake [4]. Such flows exist around heavy vehicles such as tractor-trailers, buses and high-speed trains. They also exist behind road vehicles and it is estimated that aerodynamic drag is responsible for at least 60% of total fuel consumption for the typical car on the motorway [8, 19]. Consequently, there is a need to understand the wakes of common vehicles in order to reduce emissions which is a major contributor to air pollution.

* samareshmidya@gmail.com

In the automotive industry, standard models have been developed to study the three-dimensional wakes behind automobiles. These include the Ahmed model [1], the MIRA model [3], the SAE model [15], and the DrivAer model [7]. An extensive amount of research has been conducted on the wake structure based on the Ahmed model, which is a parallelepiped with a streamlined front part and a slanted surface at the rear. Previous studies of the wake behind the Ahmed body have shown the existence of a well-defined separation bubble over the slanted surface, a pair of counter-rotating longitudinal vortices (C-pillar vortices) at the two side edges of the slanted surface, and two recirculation bubbles behind the trailing surface [1, 11, 13, 14, 17, 32]. The longitudinal vortices are considered to be highly stable [12, 29] whereas the 3D wake behind the rear base is related to 3D vortex shedding [23, 33]. It is the slant angle ϕ, nonetheless, that has the largest influence on the drag. For example, for an Ahmed body, with a given leading edge curvature, the drag has a minimum around $\phi = 15^0$ and a maximum at a critical angle $\phi = 30^0$, after which the drag drops sharply [1].

In an effort to reflect the aerodynamic shapes of modern cars, the DrivAer model was introduced based on the geometry of two cars: the Audi A4 and the BMW 3 Series [7]. Unlike the Ahmed body, the model consists of characteristic curves of modern cars and can include external structures such as wheels and rearview mirrors among others. References [9] and [25] compared using computational fluid dynamics (CFD) the aerodynamic forces and wake structure for three different configurations of the DrivAer model: squareback, fastback and notchback. Due to the complexity of the model geometry, the former study employed very large eddy simulation (VLES) and latter Reynolds-averaged Navier-Stokes (RANS) to obtain the time-averaged flow. Other studies [2, 6] have investigated the wake using detached-eddy simulation (DES). It was concluded that RANS models struggled to capture the correct flow field even with fine meshes due to an under-prediction of turbulence levels in the initial separated shear layer. This study uses a multi-wake model [24], which shares features of the Ahmed body and DrivAer model. It emulates the aerodynamic wake characteristics of different vehicles classes.

Even though experimental approaches have an advantage in that they do not rely on modeling assumptions, it is challenging to characterize three-dimensional wakes. References [26, 31, 34] performed experiments that focused on the pressure and forces of the DrivAer model under various free-stream conditions. The first particle image velocimetry

(PIV) measurements investigated the velocity field on the center plane behind the upper slant [27]. Three-dimensional PIV was performed by Ref. [16] who reconstructed the mean (time-averaged) wake using planar measurements in $x-z$ planes and $y-z$ planes where x, y, and z are the streamwise, wall-normal, and spanwise directions, respectively. The study concluded that the formation of C-pillar vortices can be delayed using a notchback configuration thus inhibiting the formation of the main recirculation bubble behind the body.

Previous studies have shown that the wake of a bluff body is almost always dominated by several unsteady features [30, 36]. A considerable portion of wake turbulent energy is coherent. As one example, low-order models constructed from a limited number of proper orthogonal decomposition (POD) modes successfully capture the main wake dynamics of axisymmetric wakes [22] and squareback Ahmed bodies [21]. It is important to understand the nature of these structures for successful control of a turbulent bluff body wake, e.g. Refs. [5, 35]. For the multi-wake model, it is first necessary to identify the most significant mean structures inhabiting the wake. In this study, the wake of a multi-wake model [24] is investigated. It contains a lower slant angle which significantly modifies the wake. All three velocity components of the mean wake are measured at multiple $y-z$ planes and the full wake is reconstructed by stacking together all planes of measured data. The effects of both the upper and lower slant edges on the development of the recirculation bubble behind the model and its far wake can thus be identified.

The rest of the paper is organized as follows. Section II provides details about the experimental facilities and the stereo-PIV used to measure the wake. Section III describes the mean flow structures and the evolution of the wake which can be split into two regions. The first is immediately behind the body where the flow is dominated by a recirculation bubble. The second is the wake behind the recirculation bubble where corner vortices, often referred to as C-pillar vortices in the literature, dictate the wake dynamics. Finally, Sec. IV discusses the conclusions and future work.

II. EXPERIMENTAL FACILITIES AND APPROACH

Figure 1 shows the front and side view of the multi-wake model, hereafter referred to as the model in the interest of brevity, along with dimensions in millimeters (more details about practical uses of the model can be found in Ref. [24]). The surface and skeleton of the body

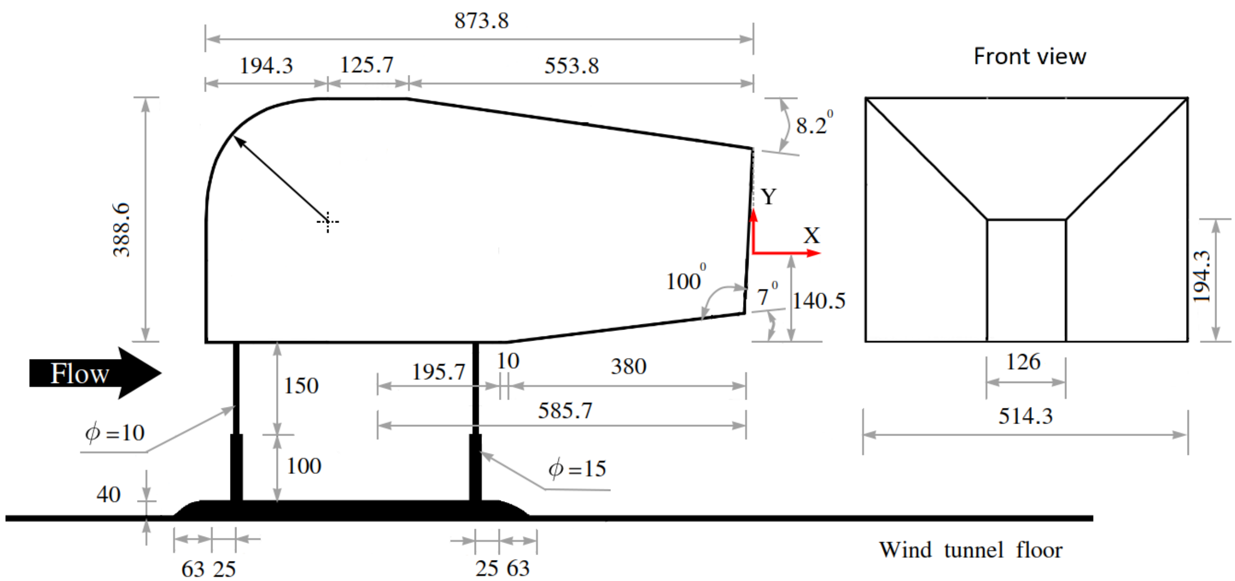

FIG. 1. Side and front views of the model with its dimensions reported in millimeters.

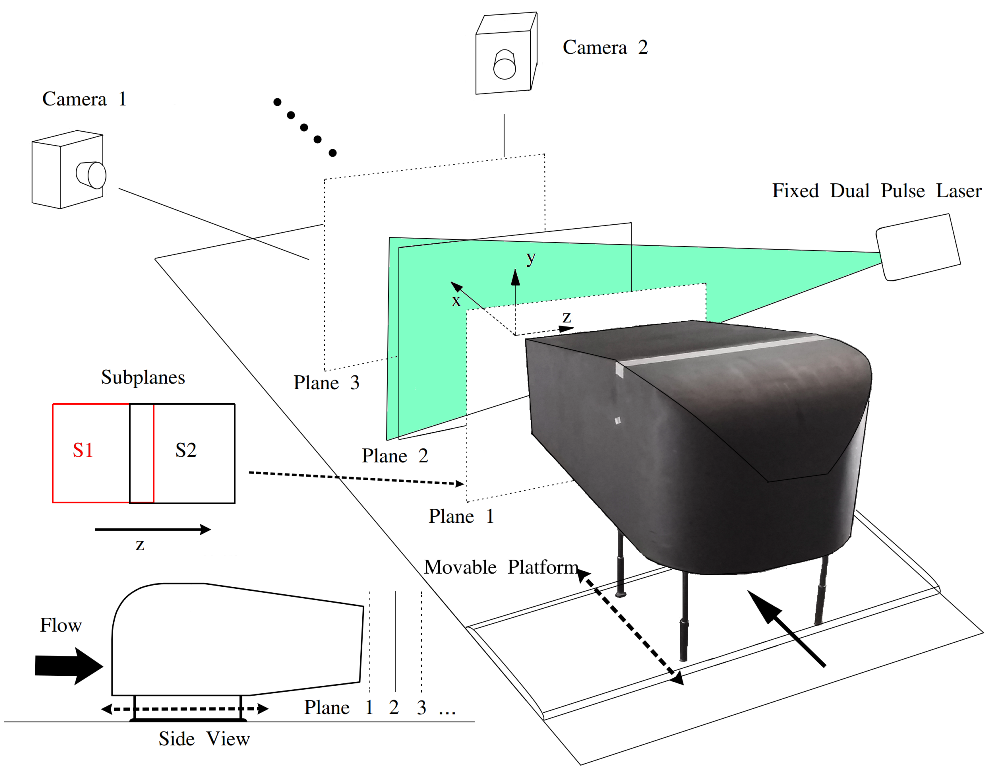

FIG. 2. Schematic of the experimental setup. The streamwise position of the model can be adjusted to measure the velocity field in various vertical-spanwise planes.

are made of plywood and aluminum, respectively. Experiments to measure the wake are

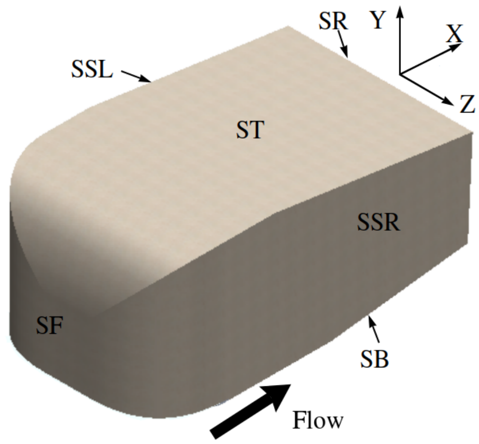

FIG. 3. Different surfaces of the model with their acronym.

conducted in the R. J. Mitchell wind tunnel at the University of Southampton. The tunnel is a closed-return facility with a working section of 3.6 $m \times 2.4\ m \times 10\ m$, speed range of $4-40\ m/s$ and a working section free-stream turbulence level of less than 0.2%. An air chiller is also included in the wind tunnel to regulate the airflow temperature. A free-stream velocity of 10 m/s is employed for wake generation. The nominal streamwise length-based Reynolds number is $Re_L = 5.64 \times 10^5$ (defined as $L_x U_\infty/\nu$, where L_x is the nominal streamwise length of the model, U_∞ is the free-stream velocity, and ν is the kinematic viscosity). The normalized quantities are denoted with a superscript * (e.g., $U^* = U/U_\infty$, $x^* = x/L_x$) and the relevant parameters of the experiment are shown in Table I.

To minimize laser reflections, the entire model and its supports are painted black. As seen in Fig. 2, the model is mounted on a movable platform using four cylindrical columns. In order to allow the body's wake to freely evolve, the diameter of these supports is kept as small as feasible. The platform is attached to a cross rail that is mounted to the tunnel floor. The cross rail is also painted black to stop laser reflections and allows for the streamwise position x of the model to be adjusted. The streamwise distance of the rail from the wind tunnel leading edge varied between $100-1200$ mm, which produces a maximum boundary layer height of $O(35mm)$. The bottommost surface of the model was placed at a height of 290 mm from the wind tunnel floor to make sure there is no effect of the boundary layer on the wake dynamics. Vertical-spanwise planes are illuminated by a dual pulse laser while smoke particles are used to seed the flow.

TABLE I. Parameters of the experiment.

$U_\infty(m/s)$	$L_x(m)$	Re_L	$h_R(m)$	$w_R(m)$	$A = h_R/w_R$
10	0.874	5.64×10^5	0.260	0.514	0.505

In order to increase the measurement resolution, two experiments are conducted that capture subplanes S1 and S2 as shown in Fig. 2. The dataset for each subplane is processed separately and stitched together to obtain the velocity field at each streamwise location. The laser plane's position is kept fixed since the model can be shifted in the streamwise direction using the aforementioned cross rail. As such, only a single PIV calibration is necessary to obtain the velocity field at various streamwise ($x = 11 - 1011$ mm, with a step of 100 mm) locations. Fig. 3 shows the names of the different surfaces of the model. The $x - y$ origin of the global coordinate system is shown in Fig. 1. The x-location of the origin coincides with the x-location of the trailing edge, and the y location is at a height of 140 mm from the horizontal portion of the surface SB. The z location coincides with the mid-spanwise plane (i.e., the plane of symmetry).

The specifications of the Stereo-PIV system are as follows. Two cameras with identical specifications are used for the measurements. The resolution of the camera is 5312×4600 with pixel size 2.7 $\mu m \times$ 2.7 μm, giving a sensor size of 14.3 $mm \times$ 12.4 mm and a 448 mm wide and 405 mm high field of view (FOV). The viewing angles of the cameras varied between $\approx 35^0$ and 40^0. Both cameras have similar lenses with a focal length of 50 mm and operate with an aperture of $f/2.8$. The wake's cross-plane ($y - z$), where y is the vertical direction and z is the spanwise direction, is illuminated by a dual-pulse laser (sheet thickness 2 mm) while smoke particles are used to seed the flow. A fog generator is used to generate smoke particles with a nominal diameter of $O(1.5\ \mu m)$. A Neodymium-doped: Yttrium Aluminum Garnet (Nd: YAG) laser with an energy of 200 mJ, a frequency of 15 Hz, a laser beam duration of 6 ns, and a wavelength of 532 nm is used to illuminate the crossplane ($y - z$ plane). An in-house PIV code is used to process the images with an initial 128×128 pixel interrogation window and a final 48×48 pixel interrogation window with 5 passes (48×48, 3 times) and a 75% overlap between the windows. The initial processing of the images is done using a POD filter [18]. The Stokes number calculated is well below 1 ($St = \rho_p d_p^2 U_\infty / 18\mu_a h_R$, where ρ_p is the density and d_p is the diameter of the fog particle, μ_a is the dynamic viscosity of the air, and h_R is the height of the rear face vertical projection), which ensures the accuracy of the flow measurements. A total of 200 instantaneous snapshots are taken for each subplane and used to obtain the mean statistics. The final spacing of the vector grid of one velocity vector in the time-averaged velocity map is $dy \times dz = 0.857 \times 0.939\ mm^2$. Whenever necessary, digital masks are used to exclude bad regions of the images.

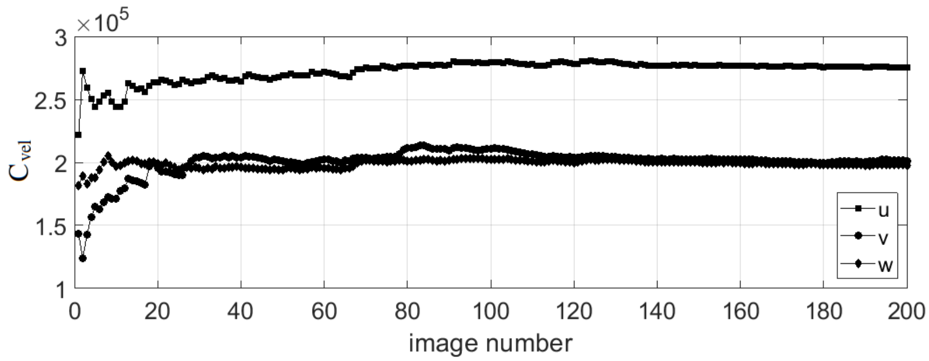

FIG. 4. Convergence of the C_{vel} norm of all velocity components for subplane S_2, $x^* = 0.357$.

The mean velocity in each direction is converged fully for each subplane, and Fig. 4 shows a convergence metric norm (defined as $C_{vel} \equiv \frac{1}{i}\sum_{i=1}^{i}(\sum\sum u_{jk} * u_{jk})^{1/2}$ where u represents a velocity component, i represents the number of images, j represents the vertical, and k represents the spanwise direction) for location $x^* = 0.242$. As mentioned earlier, the dataset for each subplane is processed separately, and all the results presented for a full crossplane are obtained by stitching the subplane results. A linear combination of the mean velocities of each subplane is used to obtain the velocities at the overlap region. The procedure is schematically shown in Fig. 5 and can be mathematically written as

$$S_{12} = w_{s_1} S_1 + w_{s_2} S_2, \tag{1}$$

$$w_{s_1} = \begin{cases} 1 & \text{if } z \leq z_{s_2} \\ \frac{z_{s_1} - z}{z_{s_1} - z_{s_2}}, & \text{if } z_{s_2} \leq z \leq z_{s_1} \\ 0 & \text{otherwise,} \end{cases} \tag{2}$$

$$w_{s_2} = 1 - w_{s_1}, \tag{3}$$

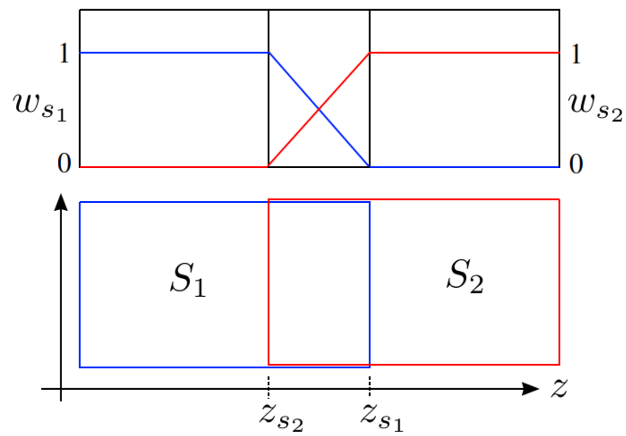

FIG. 5. Stitching technique of two subplanes.

where z_{s_1} and z_{s_2} represent the edge of the subplanes S_1 and S_2, respectively (Fig. 5). A full 3D-3C mean flow field of the full wake is constructed by stacking the velocities of these planes.

III. RESULTS

All the results are presented in terms of normalized quantities. U, V, and W represent the streamwise, the vertical, and the instantaneous spanwise velocity, respectively. The velocity field can be Reynolds-decomposed into a mean and fluctuating component, i.e. $U = \overline{U} + u$), where an overbar $(\bar{\cdot})$ represents the mean component and a lower-case letter denotes a fluctuating component. The aspect ratio A is defined as the ratio of the height and the width of the rectangle obtained from projecting the model back face onto the $x-z$ plane. The aspect ratio in the current experiment is set at 0.505. Future studies should consider exploring its effects, as it can significantly influence the evolution of the wake, particularly in the far wake region.

A. 2D MEAN VELOCITY FIELDS AND SYMMETRIES

This section considers two-dimensional slices of the mean velocity field to establish symmetries in the flow. Figure 6 shows all velocity components at plane $x^* = 0.127$. There are some striking features that can be observed. To begin with, it can be noted that the

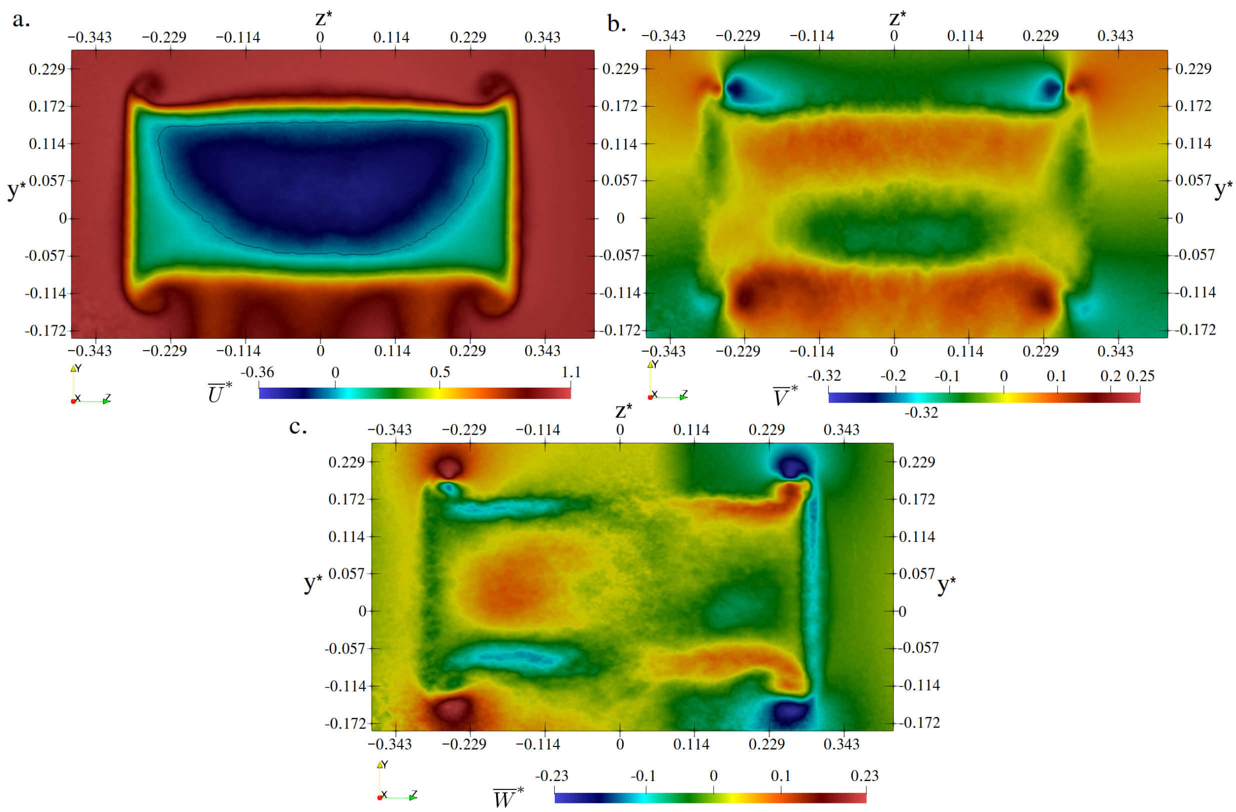

FIG. 6. Components of mean velocity at $y - z$ plane $x^* = 0.128$. The $\overline{U}^* = 0$ contour is shown with a solid black line.

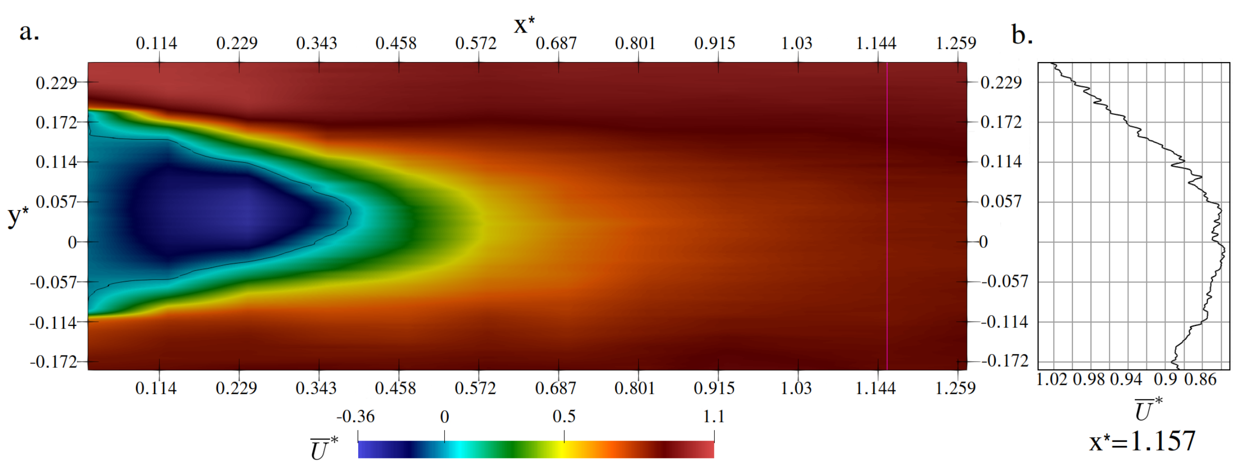

FIG. 7. a. Mean streamwise velocity on the mid $x - y$ plane ($z^* = 0$). The $\overline{U}^* = 0$ contour is shown with a solid black line. b. Also shown a sample velocity profile on the plane at $x^* = 1.157$.

streamwise and vertical velocity components are symmetric whereas the spanwise velocity component is anti-symmetric with respect to the $z^* = 0$ plane. The near-perfect symmetry

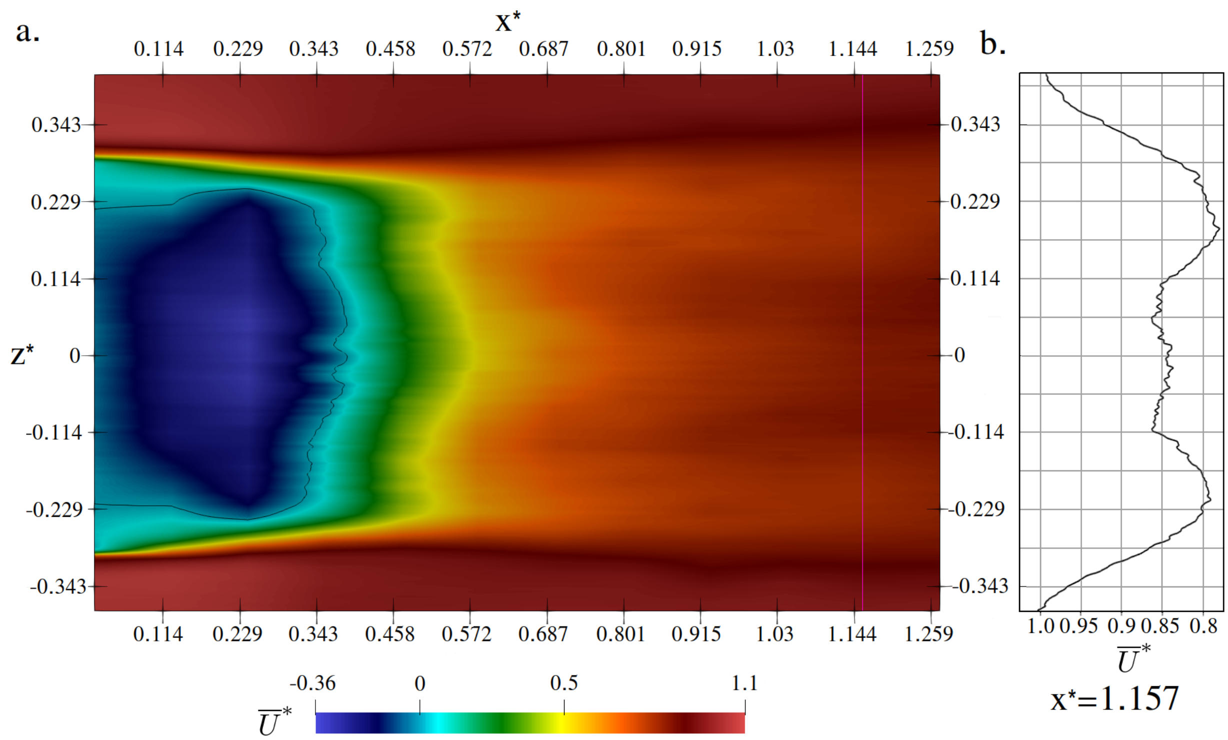

FIG. 8. a. Mean streamwise velocity on the $x - z$ plane approximately passing through the tip of the seperation bubble ($y^* = 0.04$). The $\overline{U}^* = 0$ contour is shown with a solid black line. b. Also shown a sample velocity profile on the plane at $x^* = 1.157$.

and anti-symmetry of the velocity fields validate that all the processes from model designing to the data processing have been done with the required accuracy at all measurement planes. Figure 6a also hints at the presence of several dominant structures in this plane which are discussed in greater detail in Sec. III B.The near-rectangular cross-section of the wake is clearly visible at this streamwise location. Moreover, the negative streamwise velocity in the inner region, demarcated by the $\overline{U}^* = 0$ contour, indicates the presence of a recirculation zone. Figures 6b and c indicate that the flow internal to the bubble is completely 3D in nature. The region below the main wake carries a clear signature of the four supports. Even though the effect of the supports is visible in the streamwise velocity, Figs. 6b and c suggest that their influence on the vertical and spanwise velocity components is negligible. Finally, the combination of all three velocity components indicates the presence of a concentrated vorticity region at each of the wake outer corners.

Figure 7a shows the mean streamwise velocity on the $x - y$ plane at $z^* = 0$, and Fig. 8a shows the same on an $x - z$ plane with $y^* = 0.04$. This planar information is obtained by

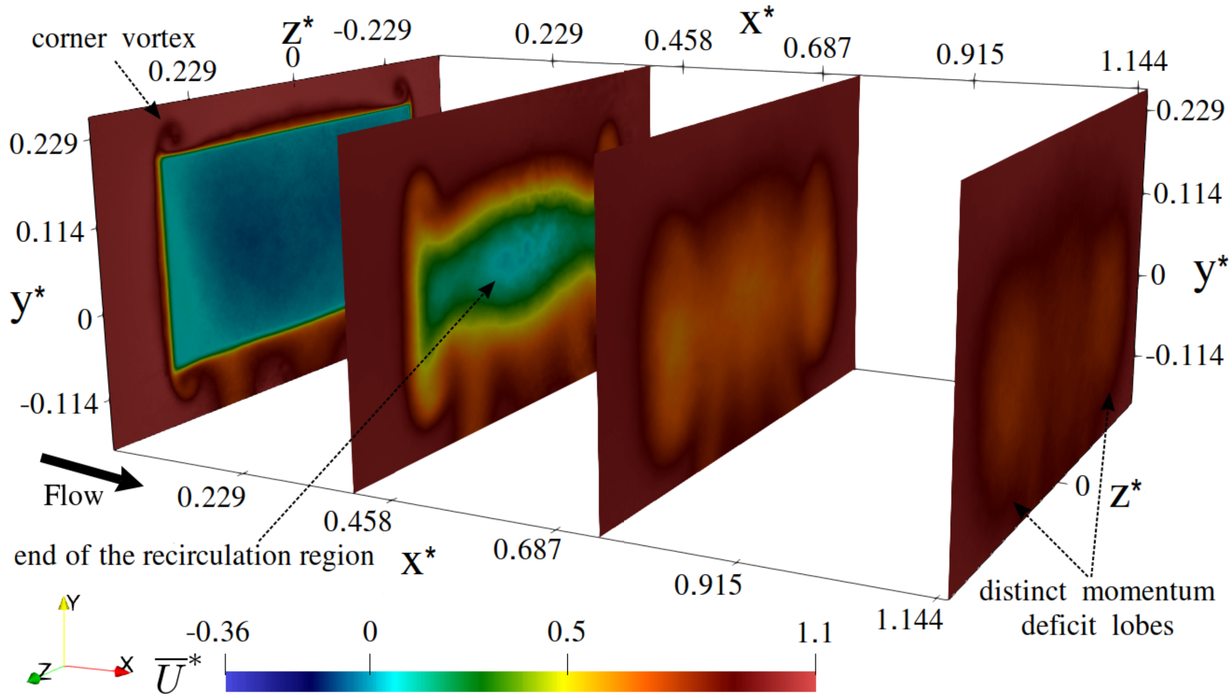

FIG. 9. Streamwise velocity components at four ($x^* = 0.014,\ 0.4,\ 0.744$ and 1.157) succesive $y - z$ planes.

taking a slice from the 3D flow field and using linear interpolation to reconstruct the missing data. For each plane, a velocity profile along the line $x^* = 1.157$ is also shown to make clear the symmetries of the wake. Figure 7a demonstrates that just downstream of the model there exists a region with negative velocity, which indicates the presence of a separation bubble. This bubble does not have an $x - z$ plane of symmetry. This lack of symmetry is a consequence of differences in ST and SB face upstream conditions and their slant angles. There is also the existence of a slant in surface SR. A visual inspection of the late evolution of the wake shows that it travels downward. On the other hand, Fig. 8a demonstrates that the mean streamwise velocity in the $x - z$ plane is symmetric about $z^* = 0$. Figure 8 also gives some insight about the complex 3D nature of the separation bubble. The late evolution shows that the wake can be broadly divided into three different segments. The first is the bubble region, the second is the region where the velocity deficit is divided into three separate regions, and the third region is where the velocity deficit at the center is smeared out resulting in two deficit regions (as seen by the profile at $x^* = 1.157$. The reason behind such behavior will be analyzed later in detail.

To further clarify the central features of the full wake, Fig. 9 shows the mean streamwise velocity ($\overline{U}$) at four successive ($x^* = 0.014,\ 0.4,\ 0.744$ and 1.157) streamwise planes. The selection of these planes aims to illustrate the scope of the primary mean features of the flow. The first plane is immediately downstream of the face SR, where the wake is almost rectangular in shape and mimics the vertical projection of the face SR. The second plane is chosen where the mean streamwise velocity attains a zero value and indicates the end of the recirculation region. It also shows how the region with the highest momentum deficit starts deforming. The third plane represents a region where the wake has recovered a significant amount of momentum and has been divided into three almost distinct momentum deficit regions. By the fourth plane, the middle region has recovered more momentum, resulting in two symmetric (about $z^* = 0$) low momentum lobes. Each plane contains some signature of the momentum deficit introduced by the supports although they are small.

B. 3D MEAN VELOCITY FIELD AND STRUCTURES

Having analyzed the mean velocity field from a two-dimensional perspective, this section investigates the structures present in the three-dimensional velocity field. The most dominant and easily identifiable structures are a separation bubble containing a recirculatory flow present in the near-wake of the model and four corner vortices, each originating at a slant face-flat face junction. The near-wake region's dynamics are dominated by the separation bubble which is analyzed in Sec. III B 1. The far-wake region's dynamics, meanwhile, are dominated by the corner vortices which are investigated in Sec. III B 2

1. Recirculation Zone / Separation bubble

Although there is no specific definition of a 3D separation bubble, it can be expected that it corresponds to a closed (or almost closed, as they can exchange fluid with outer regions) 3D topology. With the available dataset, two separate criteria are used to visualize the shape of the separation bubble. At first the mean streamlines are used to visualize the structure of the bubble. Several random points in the near-wake region are chosen, and the 3D streamlines passing through them are calculated. The Runge-Kutta 4-5 integration method is chosen to extend the streamlines which are illustrated in Fig. 10. The mean bubble shape can be clearly distinguished using the spiraling streamlines. A streamwise velocity threshold criteria ($\overline{U}^* \geq 0.75$) is used to reduce the opacity of the outer streamlines and facilitate visualization of the streamlines that pass through the bubble. The streamlines are also colored using the streamwise velocity. This provides a clear representation of the reverse flow region shown previously in Figs. 7 and 8.

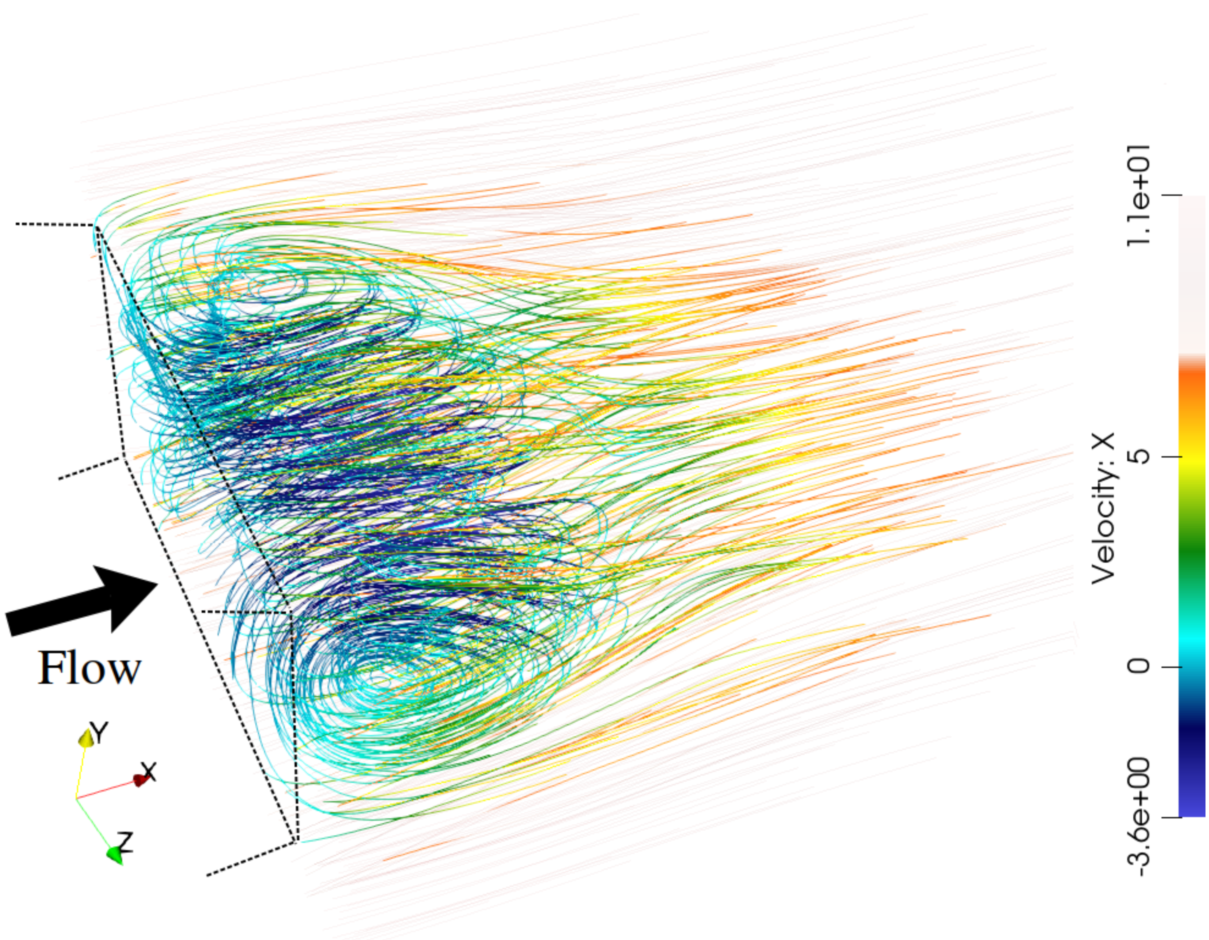

FIG. 10. The streamlines coloured by the streamwise velocity just downstream of the model.

The bubble starts at the trailing perimeter of the model (assuming there is no separation at the top and bottom trailing edges) and extends up to streamwise location $x^* = 0.4$. Consistent with Figs. 7 and 8, the streamlines show an overall symmetry about the $z^* = 0$ plane, and there is no $x - z$ symmetry plane. Figure 11 shows two different views of the bubble. Figure 11a shows the streamlines when the $x - y$ plane is viewed at $z^* = 0$, and Fig. 11b shows the streamlines in an $x - z$ plane at $y^* = 0.04$. The streamline patterns further demonstrate the symmetry property of the flow. The $x - y$ plane streamlines are

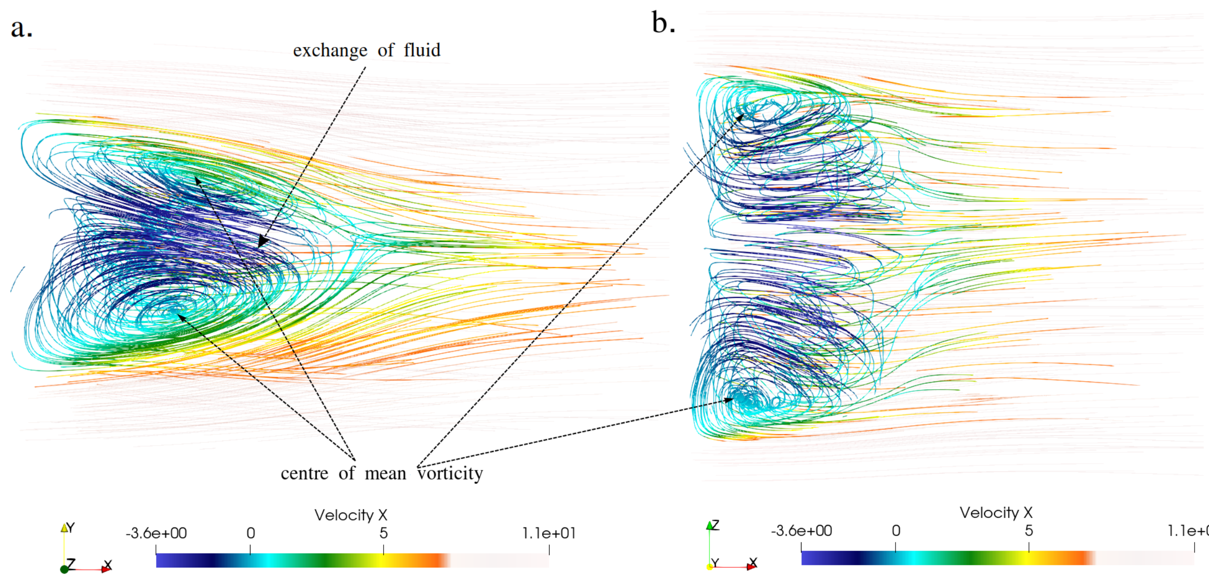

FIG. 11. The streamlines when viewed from normal to cuts. a). Cut at $z^* = 0$. b). Cut at $y^* = 0.04$.

clearly not symmetric, with the bottom eddy having a larger vertical extent and a center located slightly nearer to the body. The top eddy is relatively elongated in the streamwise direction, with its center positioned further away from the model. The mean streamline patterns also suggest that these two eddies are not completely disconnected and exchange fluid among them. The $y - z$ plane view, on the other hand, shows a near-perfect symmetry. These two figures demonstrate that these streamlines are 3D in nature, and they indicate the presence of a 3D vorticity field. Next, the dominant mean vorticity cores are extracted.

The λ_2 criterion [10] is applied to the 3D mean velocity field to identify the vortex cores, and the result is shown in Fig. 12. Inside the bubble, there exists a large single vortex that is formed due to the connected vorticity of the shear layer detached from the perimeter of the body. In the current article, this mean vortex will be called a 'bound vortex.' As can be seen in Fig. 12, the bound vortex has a complex 3D topology, and its core location is directly related to the strength of the detached shear layer. Figure 13 shows different sections of the bound vortex. Immediately downstream of the model, the bound vortex-induced flow tries to stretch the size of the separation bubble in all directions. The boundary layer developed on the faces SSR and SSL will be relatively thin owing to the zero pressure gradient (hereafter referred to as ZPG), and that leads to a higher mean shear. This relatively thin, higher shear region will separate and morph into a concentrated vortex and will remain relatively nearer to the body (in comparison to the top and bottom vortex cores). The shear will also be symmetric on these two sides.

In contrast, the flow at the surfaces ST and SB will initially encounter a ZPG, but once the slant starts, the flow will experience an adverse pressure gradient (hereafter referred to as APG). On the SB side, the flow will separate at the sharp leading edge and will reattach downstream of the local separation bubble. The slant at face SB starts later than that of face ST, and the angle (7°) is smaller. This makes the effect of the APG less severe on the boundary layer developed on face SB and keeps the flow attached until the trailing edge. This manifests in a well-defined, concentrated vortex core on the bottom side and can be seen in Fig. 13b. On face ST, the boundary layer will face a longer length of APG likely triggering separation before reaching the trailing edge. This leads to a less concentrated, fluctuating vortex core. Relatively less shear at faces SB and ST (which cannot be confirmed experimentally) pushes the vortices generated from these two faces stay further away from the body. The final vortex core detached from the trailing perimeter takes a complex 3D shape as shown in Fig. 13a. In the near wake, the bound vortex plays a dominant role and dictates the nature of the internal flow of the separation bubble. The slight tilting angle of face SR will make sure that there is a downward tilt on the bound vortex core. In addition, the effect of differential trailing edge shear at surfaces ST and SB further tilts the vortex chain. This effect can be seen in Fig. 14. Although the back face inclination angle is 3°, the bound vortex inclination angle is considerably higher and is $\approx 15°$.

2. Corner Vortices and their evolution

The second important feature of the wake is the corner vortices. There are four of them present at each corner of the flow, as shown in Fig. 15, extracted using the λ_2 criterion. Figure 16 illustrates the variation in the maximum absolute streamwise vorticity of the corner vortices along the streamwise direction. The corner vortices play an important role in the evolution of the wake.

a. Effect on evolution of the near wake:

In this section, vertical-spanwise $(v - w)$ velocity vectors and streamwise $(y - z$ plane$)$

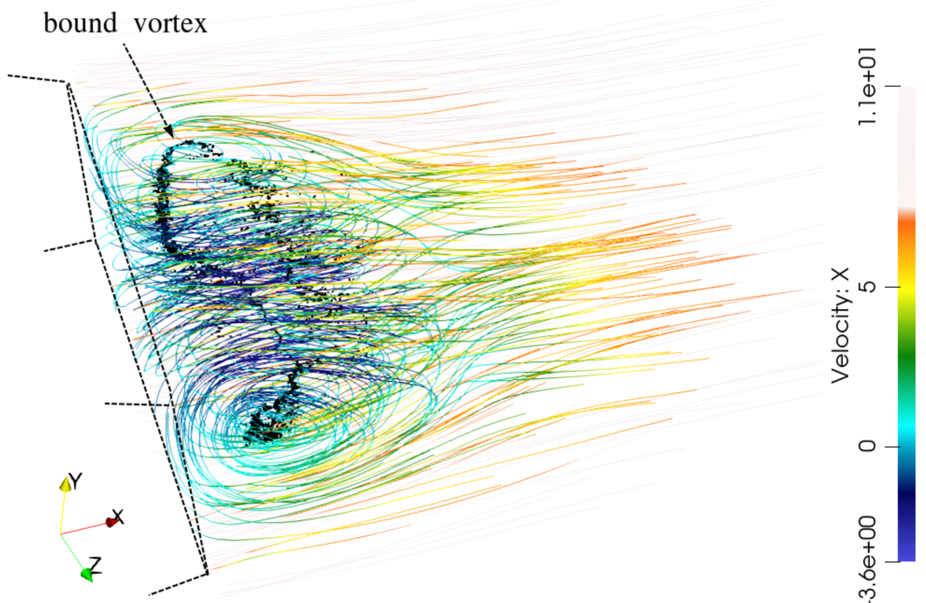

FIG. 12. Position of the bound vortex with respect to the model. The streamlines are also shown.

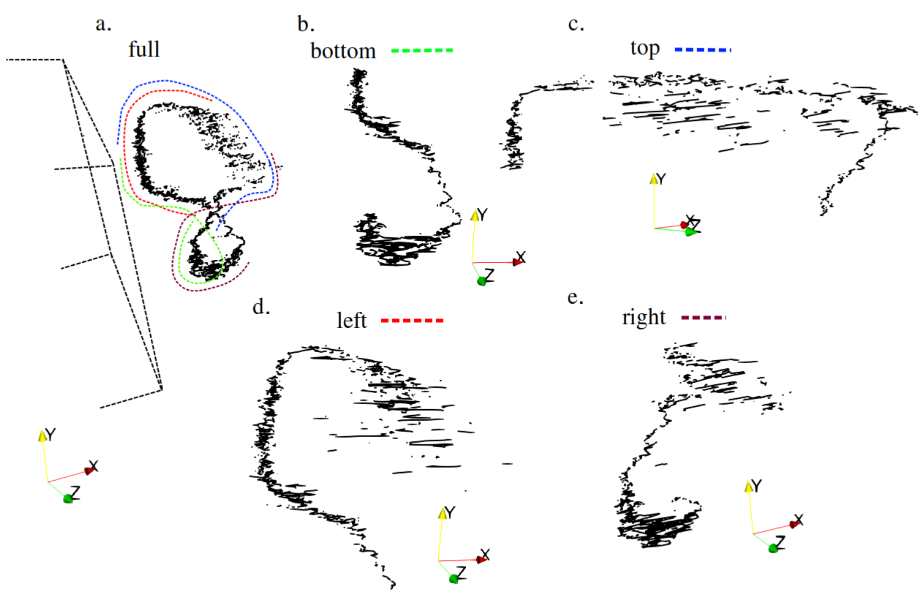

FIG. 13. Isometric views of the bound vortex core. a. The full core. The colours are used to highlight the four sides in the full core view and are presented separately for a better viewing angle.

vorticity are used to demonstrate how the flow in the wake changes in the streamwise direction. Figure 17 shows the velocity $v - w$ vector plots with normalized streamwise vorticity overlaid on top. The vorticity magnitudes are shown on alternate figures so that

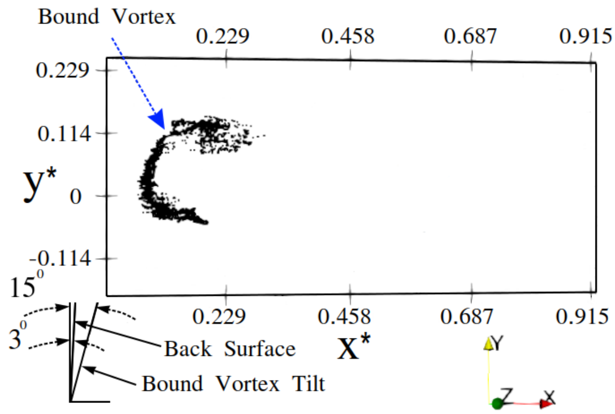

FIG. 14. Side view of the bound vortex core. The mean inclination, defined based on the tilt of the central regions of the two well-defined side cores of the bound vortex in the $x-y$ plane ($\approx 15°$), is noticeable and is different from the back face slant angle ($3°$ off from the vertical) of the model.

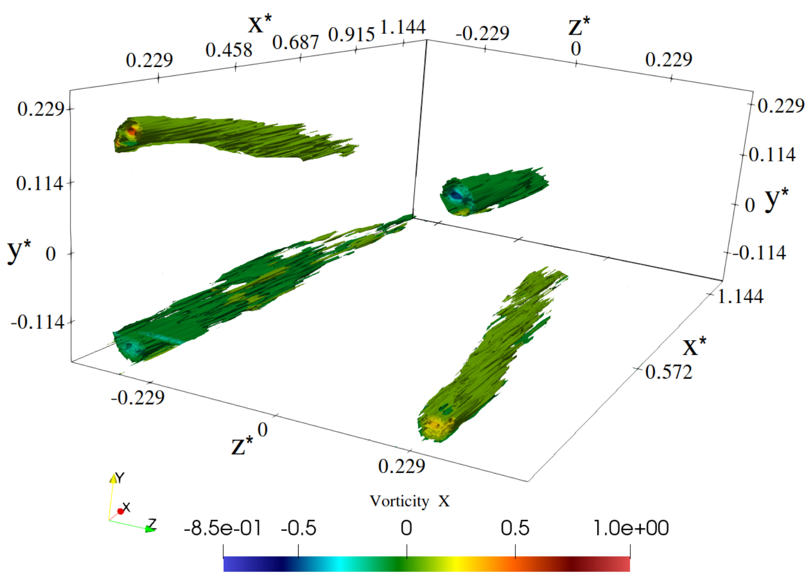

FIG. 15. The corner vortices. Coloured by the x-vorticity.

it is possible to clearly understand the effect of the vortical structures on the streamwise evolution of the $v-w$ velocity. Plane 1 shows the existence of strong, relatively compact corner vortices. It also shows that the flow inside and outside the bubble can be separated completely, which is indicative of little direct interaction between the bound vortex and the corner vortices. At Plane 1 the internal flow of the separation bubble is going outward (Fig. 17a) in all directions. At first this might seem counterintuitive since the pressure inside the bubble will be less than that of the free stream. As such, the gradient of pressure will

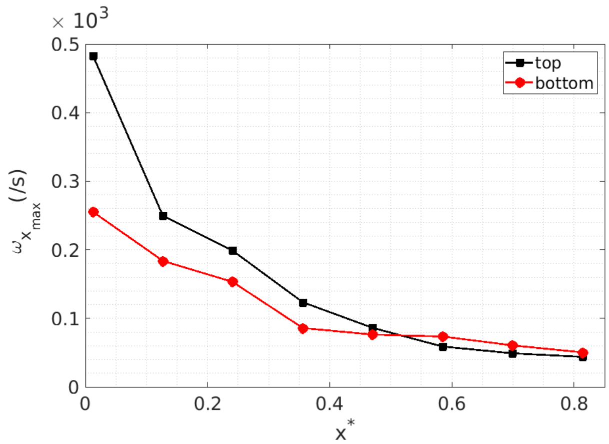

FIG. 16. Streamwise evolution of maximum absolute vorticity of top and bottom corner vortices. The result is averaged over two equal-strength but counter-rotating vortex pairs.

be inward and the bubble will try to suck the flow from all directions. The flow in Fig. 17 is nonetheless consistent with the closed-loop nature of recirculation bubbles and location of the bound vortex core, which is further downstream of this plane. The resulting shape of the wake is an almost perfect rectangle as seen in Fig. 17a.

In Plane 2, flow at the central regions of the periphery of the wake has developed an inward component and is consistent with the overall pressure difference between the free stream and the wake. The corner vortices are larger and the internal $v - w$ flow shows a complex shape. At this plane, almost all the inner flow at the top and the bottom is going outward as before, but on the sides the flow has changed direction. Figure 17b shows the existence of four different internal cells at four quadrants. This corresponds to the effect of pressure and the complex 3D shape (and tilting) of the bound vortex core. The side cores of the bound vortex reside between the Planes 1 and 2, whereas the top and bottom parts of the vortex core reside mostly between the Planes 2 and 3 (Fig. 14). On the sides, the bound vortex effect dominates and tries to move the fluid in the inward direction, whereas in their vicinity, the corner vortices try to move the fluid in the outward direction. The situation is a little different on the top and bottom sides. On these two sides, the bound vortex tries to move the fluid in the outward direction, whereas the corner vortices try to move the fluid in the inward direction. These combined effects create an interesting four-cell pattern at Plane 2 and start warping the wake as shown in Fig. 17b.

The bound vortex core is completely contained within Plane 3 and as a result the bound

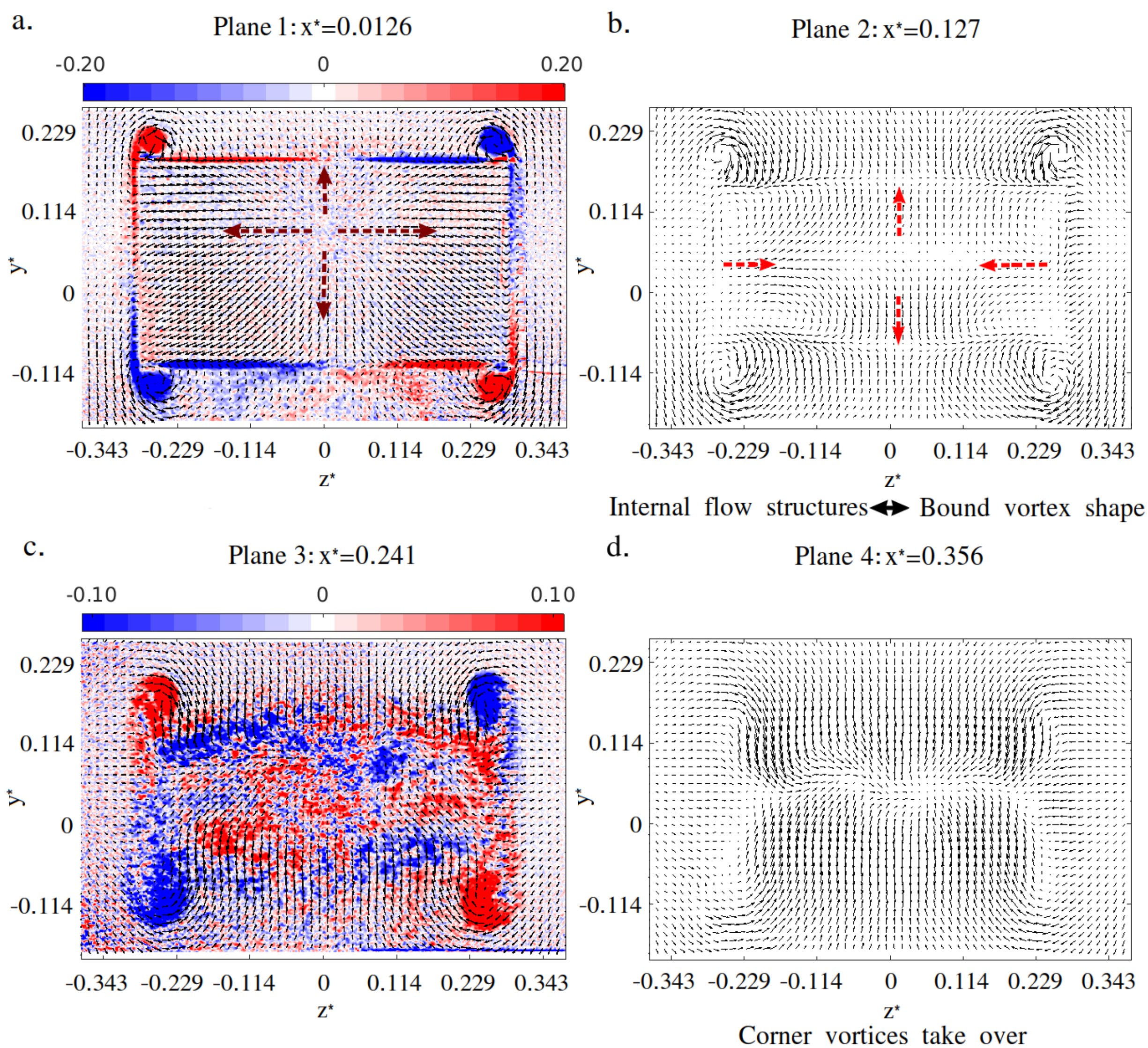

FIG. 17. Evolution of streamwise vortices in the first four planes (1-4) shown using $v - w$ velocity vector lines. Streamwise vorticity plots are overlaid on plane 1 and 3. red : $+\omega_x$, blue : $-\omega_x$. The arrows at planes 1 and 2 highlight the dominant flow directions. The vorticity values are normalized using the averaged absolute maximum vorticity of top side corner vortices of the first plane ($\omega_{x_{max}} = 0.483 \times 10^3\ /s$).

vortex-induced flow tries to go inward in all directions at Plane 3. By this time, the corner vortices diffuse further and become larger. In their immediate vicinity, on the sides (i.e., SSL and SSR), they try to move the fluid outward and counter the inward flow. In these areas (i.e., the top and bottom regions of the sides), these opposing effects stop the rate of shrinking of the bubble. However, in the central region of the sides, the inward flow still dominates, causing some shrinkage of the bubble. On the other hand, the combined effects of corner and bound vortices create an inward flow at the top and the bottom sides. This flow is relatively stronger at the immediate vicinity of the corner vortices and weaker at the central region. The overall behavior is closely related to the model aspect ratio. This flow pattern creates a direction- and location-specific rate of change in the shape of the bubble. Overall, the rate of shrinkage of the bubble in the spanwise direction will be less than that in the vertical direction, and this is clearly visible in Figs. 7 and 8.

At Plane 4, the corner vortices grow further, and the overall flow pattern remains similar to that of Plane 3. However, the corner vortices almost completely block sidewise flows thus allowing flow from the top and bottom to dominate. This mismatch between the sidewise and vertical flows explains the difference in the rate of shrinkage of the separation bubble and is fully consistent with the final spanwise elongated shape of the separation bubble. These phenomena can be attributed to the aspect ratio and slant angles of the model. Plane 4 nearly coincides with the end of the separation bubble, where the central region of the wake has a near-zero streamwise velocity. From this plane onward, the corner vortices dictate the evolution of the wake. The shape of the streamlines (Fig. 12) shows that the separation bubble tip is located at $x^* = 0.4$.

b. Effect on evolution of the far wake:

Figure 18a shows that, at Plane 5, the flow is dominated completely by the corner vortices. They are significantly larger in size at this plane. The top and the bottom counter-rotating vortices start interacting on each side. At the site of their interaction, a jet-like flow appears. This is where the model aspect ratio plays a key role in deciding the nature of the wake evolution. As mentioned before, the corner vortices prevented flow from entering the vertical central region of the wake from the sides. Most of the flow coming from the top and the bottom add momentum to the spanwise central region of the wake. When compared to the other locations, the transfer of momentum is highest at this plane, which reduces the momentum deficit at a comparably higher rate at the central region.

At Plane 6, the interaction between the top and the bottom corner vortices becomes stronger and creates a strong jet-like flow (solid blue arrows). The dominance of the vortices in the evolution of the wake can be seen in later planes as well. The $v-w$ flow at the central

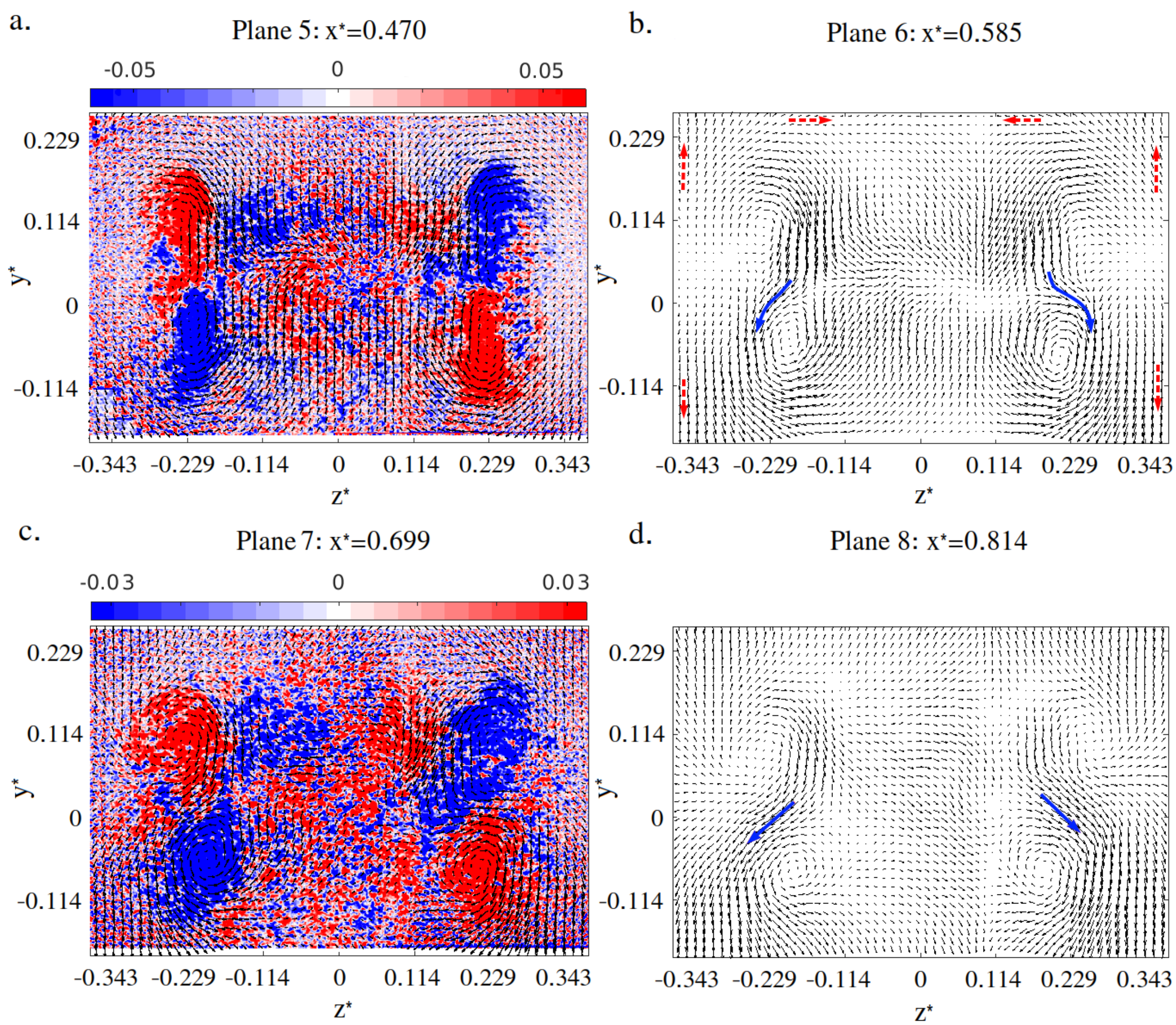

FIG. 18. Evolution of streamwise vortices in the next four planes (5-8) shown using $v-w$ velocity vector lines. Streamwise vorticity plots are overlaid on planes 5 and 7. The red : $+\omega_x$, blue : $-\omega_x$. The 'jet-like' flows arising at the confluence of the counter-rotating side vortex pairs are highlighted using solid blue arrows at planes 6 and 8 (planes 5 and 7 are excluded). The red dashed arrows highlight how, at plane 6, a significant portion of the wake peripheral flow became almost parallel to the surfaces. The vorticity values are normalized using the averaged absolute maximum vorticity of top side corner vortices of the first plane ($\omega_{x_{max}} = 0.483 \times 10^3\ /s$).

regions of the periphery of the wake has almost become parallel to the model surfaces (marked by the red dashed arrows), indicating a pressure reversal. This fact will become clearer by the next plane, where $v-w$ flow in these regions will become outward. At Plane 7, the flow in the central regions of the periphery changes direction and confirms the beginning of a new wake regime. Fig. 19 illustrates this process with greater clarity. The only possible mechanism that can produce such a change in the flow pattern must be a change in pressure. So, after the initial near-wake low-pressure (compared to the free-stream pressure) region, which includes the separation bubble, the pressure inside the wake becomes more than that of the free stream. This creates a region of outward pressure gradient. Initially this gradient will resist the already developed inward flow and finally will make the flow outward. This outward flow trend continues for the rest of the wake examined here and confirms that this high-pressure inner core persists for long. This situation will resist the inward momentum transfer thus making the velocity (or the momentum) defect persist longer in the downstream direction. Meanwhile, the jet-like flow strengthens further.

Plane 8 shows that the jet-like flow (solid blue arrows) can take fluid from the top and send it towards the bottom. In these planes, the main features are nearly symmetric. It is interesting to note that the vortices remain coherent for such a long streamwise distance. The two separate lobes, which are the signatures of the momentum deficit, visible in the mean velocity plots (Fig. 9), coincide with the two jets. Figure 20 shows the relative position of the lobes with the help of a streamwise velocity isosurface ($\overline{U}^* = 0.76$) and the x-vorticity. This indicates that as long as the previously mentioned coherence exists, the two separate regions of the momentum deficit will persist. The last plane of measurement ($x^* = 1.27$, not shown here) shows that this $v - w$ flow configuration remains dominant (albeit the effect is more diffused and uniform) further downstream. The outer flow at $x^* = 1.27$ remains outward, indicating the presence of a low momentum, high-pressure zone at the core of the wake and a spreading of the wake in each direction. For the given set of experimental conditions and the model geometry, this can be thought of as the natural state of the wake. The final vertical location of the lobes at Plane 8 shows that the wake travels downward. Calculation based on the location of the top edge of these lobes shows that this downward movement makes an angle (with streamwise direction) of $\approx 3.5°$, which is incidentally close to the back face slant angle ($= 3°$). This shows that in the long-term evolution of the wake, the bound vortex tilting does not have much influence.

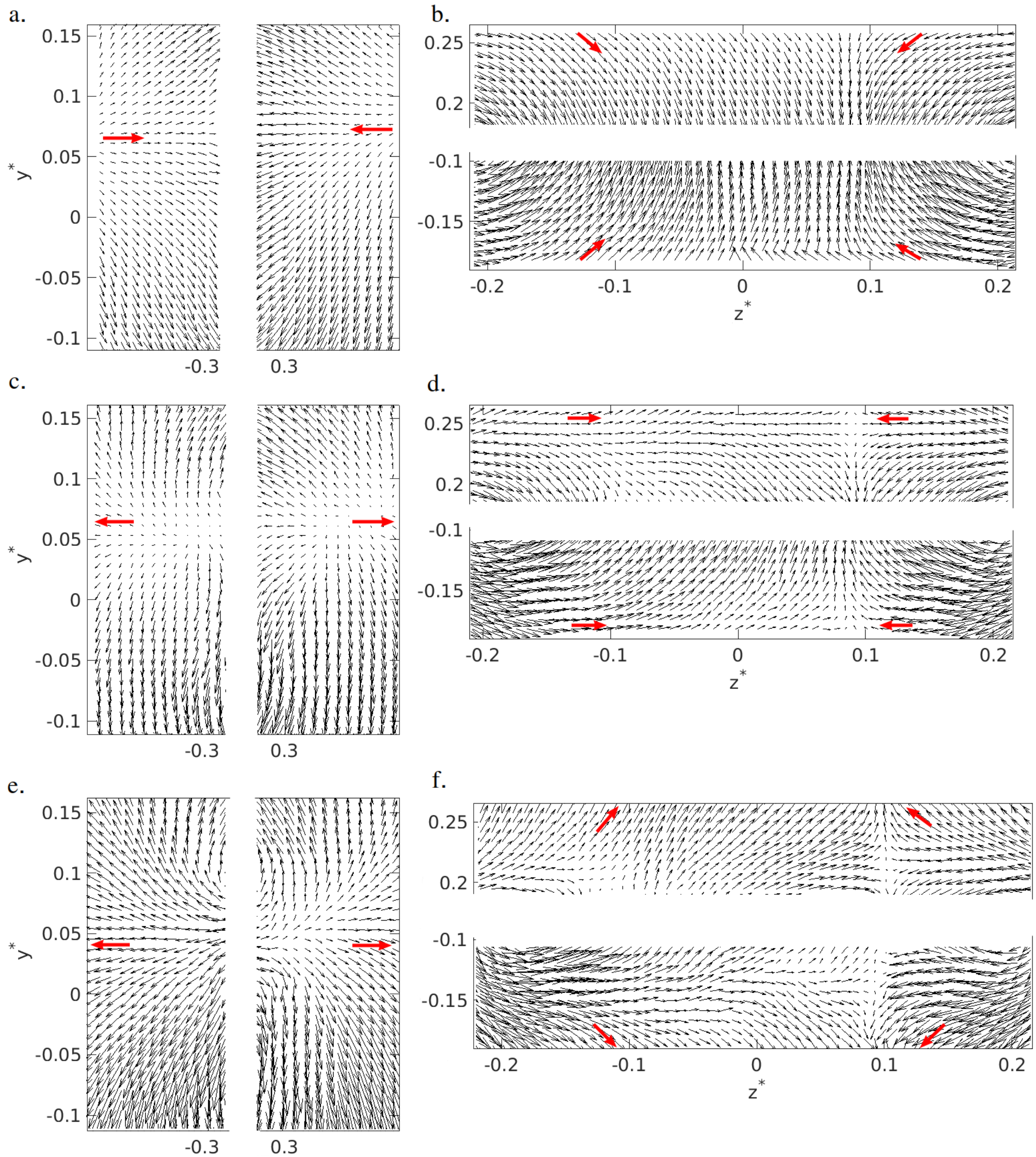

FIG. 19. Reversal of the flow at the central regions of the periphery of the wake from inward to outward. Red arrows are used to highlight the flow direction. a & b: Plane 5; c & d: Plane 6; and e & f: Plane 7.

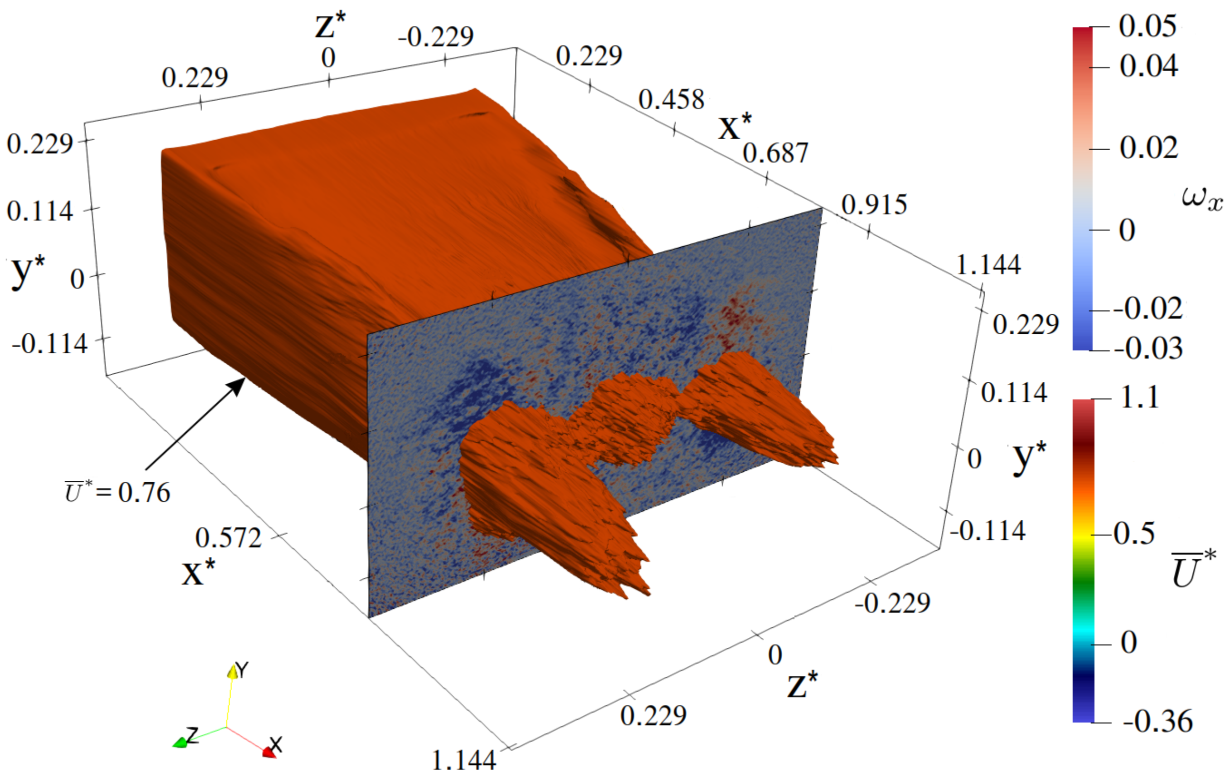

FIG. 20. Relative location of velocity isosurface $\overline{U}^* = 0.76$ and x-vorticity at plane $x^* = 0.814$.

IV. CONCLUSIONS AND FUTURE WORK

A high Reynolds number wake of a multi-wake model was examined experimentally with stereo-PIV at multiple streamwise locations. It was found that the mean flow maintains an overall symmetry up to a streamwise length of $x^* = 0.7$. The main features detected were a separation bubble, a bound vortex, and four corner vortices. These structures are similar to those behind an Ahmed body although the lower slant induced an extra pair of C-pillar vortices which modified the shape of the separation bubble as well as the far wake. The separation bubble formed immediately downstream of the model, and its mean internal flow was characterized. The shear layers detached from all surfaces of the model and morphed into a single connected 'bound vortex' which was intimately related to the internal flow of the separation bubble. The bound vortex stayed inside the separation bubble, which contained a large region of reverse flow, and dominated the flow up to $x^* \approx 0.4$. The bound vortex and the internal flows maintained a spanwise symmetry about the $z^* = 0$ axis, but no such symmetry existed in the vertical direction. The difference in the upstream condition and the presence of slant surfaces ST, SB, and SR resulted in unequal shear on the top and bottom surfaces. Due to the different upper and lower slant angles, the bound vortex was tilted in the vertical direction.

Four corner vortices formed upstream of the trailing perimeter at each slant face-flat face junction. After their formation they started influencing the flow in their immediate vicinity and continued to do so in the far-wake. In the near wake region, they enhanced the inward mass and momentum transfer in the vertical direction and opposed them in the spanwise direction. In the far wake, they redistributed the momentum in the $y - z$ plane. The overall wake could thus be split into three regions in the streamwise direction. In the near-wake, induced flow from the corner vortices warped the shape of the separation bubble at each corner without having an impact on the bubble's internal flow. Behind the separation bubble, they diffused in the spanwise-vertical plane and became larger in shape. Owing to their proximity, counter-rotating vortices on each side connected to each other and their induced flow reduced the momentum deficit in the central region, which gave the wake two separate lobes of relatively larger momentum deficit.

The dominant features of the wake provide some insight into controlling the wake to improve aerodynamic efficiency. To obtain a surface topology that produces less form drag, for example, it is desirable to have a relatively higher pressure distribution at the back face of the model. Although the streamwise resolution of the flow is sufficient to capture the wake topology, future work would be to data assimilate [20, 28] the mean velocity field to improve the flow resolution. Data assimilation could also provide information about the pressure field which was not measured in the experiments. Alternatively, the pressure field could be measured using pressuring rakes which would also provide some preliminary insight into the dominant fluctuations and their spectral content.

V. ACKNOWLEDGMENTS

The authors wish to acknowledge Dr. Renan Soares for his assistance in setting up the experiments and financial support from the Engineering and Physical Sciences Research Council (EPSRC) through grant number EP/W009935/1.

VI. APPENDIX

In this section, the circulations of the corner vortices are reported for each plane. The contours of the vorticity (streamwise) of the corner vortices are used as area domains (Ω) to obtain circulation (using $\Gamma_x = \int_\Omega \omega_x \, dydz$) in a $y - z$ plane. Using the symmetry about the $z^* = 0$ plane, the average of the absolute value of the circulation of the counter-rotating vortex pairs residing on either side is calculated and plotted. For example, two vortices that reside in the top-left and top-right corners are used for the calculation of top-side circulation. Similarly, the remaining two vortices are used for the calculation of bottom-side circulation. The contour levels are normalized using the maximum absolute averaged streamwise vorticity of the corresponding plane and side (Fig. 16). The results are shown in Fig. 21a and b.

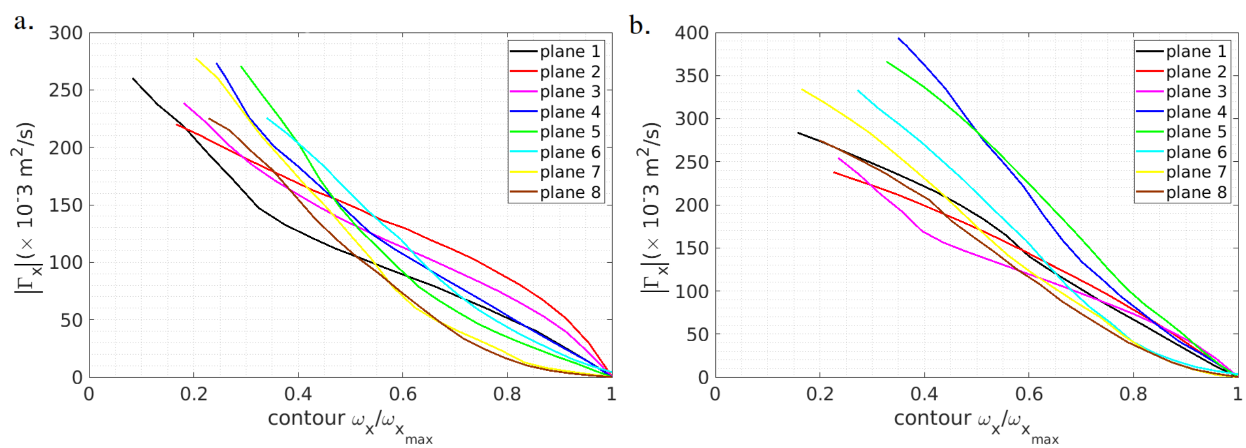

FIG. 21. Variation of the absolute circulation (averaged using two symmetric but counter-rotating vortex pairs residing on either side of the $z^* = 0$ plane) of corner vortices with streamwise vorticity levels and their streamwise evolution. a. Top. b. Bottom.

[1] S. R. Ahmed, G. Ramm, and G. Faltin. Some salient features of the time-averaged ground vehicle wake. *SAE transactions*, pages 473–503, 1984.

[2] N. Ashton and A. Revell. Comparison of RANS and DES methods for the DrivAer automotive body. Technical report, SAE Technical Paper, 2015.

[3] G. W. Carr and W. R. Stapleford. Blockage effects in automotive wind-tunnel testing. Technical report, SAE Technical Paper, 1986.

[4] H. Choi, J. Lee, and H. Park. Aerodynamics of heavy vehicles. *Ann. Rev. Fluid Mech.*, 46(1):441–468, 2014.

[5] O. Evstafyeva, A. S. Morgans, and L. Dalla Longa. Simulation and feedback control of the ahmed body flow exhibiting symmetry breaking behaviour. *J. Fluid Mech.*, 817:R2, 2017.

[6] E. Guilmineau. Numerical simulations of flow around a realistic generic car model. *SAE Int. J. Passeng. Cars - Mech. Syst.*, 7(2014-01-0607):646–653, 2014.

[7] A. Heft, T. Indinger, and N. Adams. Investigation of unsteady flow structures in the wake of a realistic generic car model. In *29th AIAA applied aerodynamics conference*, page 3669, 2011.

[8] W.-H. Hucho and G. Sovran. Aerodynamics of road vehicles. *Ann. Rev. Fluid Mech.*, 25(1):485–537, 1993.

[9] S. Jakirlic, L. Kutej, D. Hanssmann, B. Basara, and C. Tropea. Eddy-resolving simulations of the notchback 'DrivAer'model: influence of underbody geometry and wheels rotation on aerodynamic behaviour. Technical report, SAE Technical Paper, 2016.

[10] J. Jeong and F. Hussain. On the identification of a vortex. *J. Fluid Mech.*, 285:69–94, 1995.

[11] S. Krajnović. Large eddy simulation exploration of passive flow control around an Ahmed body. *J. Fluids Eng.*, 136(12):121103, 2014.

[12] S. Krajnović and L. Davidson. Flow around a simplified car, part 1: large eddy simulation. *J. Fluids Eng.*, 127:907–928, 2005.

[13] H. Lienhart and S. Becker. Flow and turbulence structure in the wake of a simplified car model. *SAE Technical Paper*, 2003-01-0656, 2003.

[14] H. Lienhart, C. Stoots, and S. Becker. Flow and turbulence structures in the wake of a simplified car model (ahmed modell). In Siegfried Wagner, Ulrich Rist, Hans-Joachim Heinemann, and Reinhard Hilbig, editors, *New Results in Numerical and Experimental Fluid Mechanics III*, pages 323–330, Berlin, Heidelberg, 2002. Springer Berlin Heidelberg.

[15] N Lindener. Aerodynamic testing of road vehicles in open jet wind tunnels. *SAE SP-1465, Warrendale*, 1999.

[16] J. Liu, Z. Zhang, Y. Wang, M. Li, and S. Xu. Experimental study on the three-dimensional wake structure of the DrivAer standard model. *J. Vis.*, 24:443–460, 2021.

[17] K. Liu, B.F. Zhang, Y.C. Zhang, and Y. Zhou. Flow structure around a low-drag Ahmed body. *J. Fluid Mech.*, 913:A21, 2021.

[18] M.A. Mendez, M. Raiola, A. Masullo, S. Discetti, A. Ianiro, R. Theunissen, and J.-M. Buchlin. POD-based background removal for particle image velocimetry. *Exp. Therm. Fluid Sci.*, 80:181–192, 2017.

[19] M. Metka and J. W. Gregory. Drag reduction on the 25-deg Ahmed model using fluidic oscillators. *J. Fluids Eng.*, 137(5):051108, 2015.

[20] V. Mons, A. Vervynck, and O. Marquet. Data assimilation and linear analysis with turbulence modelling: application to airfoil stall flows with PIV measurements. *Theor. Comput. Fluid Dyn.*, 38(3):403–429, 2024.

[21] B. Podvin, S. Pellerin, Y. Fraigneau, G. Bonnavion, and O. Cadot. Low-order modelling of the wake dynamics of an Ahmed body. *J. of Fluid Mech.*, 927:R6, 2021.

[22] G. Rigas, A. R. Oxlade, A. S. Morgans, and J. F. Morrison. Low-dimensional dynamics of a turbulent axisymmetric wake. *J. Fluid Mech.*, 755:R5, 2014.

[23] D. B. Sims-Williams and B. D. Duncan. The Ahmed model unsteady wake: experimental and computational analyses. *SAE transactions*, pages 1385–1396, 2003.

[24] R. Soares and K. Garry. The introduction of multiwake - an adaptable bluff-body wake emulator for ground vehicle studies. *SAE Int. J. Adv. and Curr. Prac. in Mobility*, 6(2):791–813, 2024.

[25] R. F. Soares and F. J. de Souza. Proposal of an aerodynamic concept for drag reduction of fastback car models. Technical report, SAE Technical Paper, 2015.

[26] D. Stoll, C. Schoenleber, F. Wittmeier, T. Kuthada, and J. Wiedemann. Investigation of aerodynamic drag in turbulent flow conditions. *SAE Int. J. of Passeng. Cars Mech. Syst.*, 9(2016-01-1605):733–742, 2016.

[27] C. Strangfeld, D. Wieser, H.-J. Schmidt, R. Woszidlo, C. Nayeri, and C. Paschereit. Experimental study of baseline flow characteristics for the realistic car model DrivAer. Technical report, SAE Technical Paper, 2013.

[28] S. Symon, N. Dovetta, B. J. McKeon, D. Sipp, and P. J. Schmid. Data assimilation of mean velocity from 2D PIV measurements of flow over an idealized airfoil. *Exp. Fluids*, 58:1–17, 2017.

[29] A. Thacker, S. Aubrun, A. Leroy, and P. Devinant. Effects of suppressing the 3D separation on the rear slant on the flow structures around an Ahmed body. *J. Wind Eng. Ind. Aerodyn.*, 107:237–243, 2012.

[30] A. Thacker, S. Aubrun, A. Leroy, and P. Devinant. Experimental characterization of flow unsteadiness in the centerline plane of an Ahmed body rear slant. *Exp. Fluids*, 54:1–16, 2013.

[31] P. Theissen, J. Wojciak, K. Heuler, R. Demuth, T. Indinger, and N. Adams. Experimental investigation of unsteady vehicle aerodynamics under time-dependent flow conditions-part 1. Technical report, SAE Technical Paper, 2011.

[32] T. Tunay, B. Sahin, and V. Ozbolat. Effects of rear slant angles on the flow characteristics of Ahmed body. *Exp. Therm. Fluid Sci.*, 57:165–176, 2014.

[33] G. Vino, S. Watkins, P. Mousley, J. Watmuff, and S. Prasad. Flow structures in the near-wake of the Ahmed model. *J. Fluid Struct.*, 20(5):673–695, 2005.

[34] J. Wojciak, P. Theissen, N. Adams, T. Indinger, and R. Demuth. Investigation of unsteady vehicle aerodynamics under time-dependent flow conditions. In *29th AIAA Applied Aerodynamics Conference*, page 3349, 2011.

[35] B. F. Zhang, K. Liu, Y. Zhou, S. To, and J. Y. Tu. Active drag reduction of a high-drag Ahmed body based on steady blowing. *J. Fluid Mech.*, 856:351–396, 2018.

[36] B. F. Zhang, Y. Zhou, and S. To. Unsteady flow structures around a high-drag Ahmed body. *J. Fluid Mech.*, 777:291–326, 2015.